Available online at www.sciencedirect.com
SCIENCE DIRECT®
ELSEVIER
Journal of Contaminant Hydrology 62–63 (2003) 577–594
JOURNAL OF Contaminant Hydrology
www.elsevier.com/locate/jconhyd

# Modeling dispersion in three-dimensional heterogeneous fractured media at Yucca Mountain

Sean A. McKenna[a,*], Douglas D. Walker[b,1], Bill Arnold[c]

[a] *Sandia National Laboratories, P.O. Box 5800 MS 0735, Albuquerque, NM 87185-0735, USA*
[b] *Duke Engineering and Services, Albuquerque, NM, USA*
[c] *Sandia National Laboratories, P.O. Box 5800 MS 0776, Albuquerque, NM 87185-0776, USA*

**Abstract**

Highly resolved numerical simulations are conducted to evaluate the longitudinal and transverse dispersivities proposed for use in the larger-scale Yucca Mountain saturated zone (SZ) site-scale model. Two different stochastic continuum models (SCM) that define the spatial variability of permeability are inferred from the observed fracture characteristics and the measured permeabilities. These models are created with a combination of indicator geostatistics and boolean simulation that allow for modeling different correlation lengths and anisotropy ratios at different permeability thresholds as well as the inclusion of large, high-permeability features. Longitudinal and transverse (horizontal and vertical) dispersion through the permeability realizations is evaluated for both distributed and focused source geometries using groundwater flow and streamline particle tracking. These numerical results are compared to behavior predicted by an analytical solution and to dispersivities estimated by an expert panel. Early time transport results are significantly non-Gaussian due to the strong heterogeneity of the fractured medium. At late times, travel distances of 23 correlation lengths, the longitudinal and transverse horizontal dispersivity results are well approximated by the analytical solution and the expert elicitation estimates. The calculated transverse vertical dispersivity values are smaller than those estimated from the analytical solution. Inclusion of high-permeability features of the same size as the model domain with a distributed planar source creates extreme values of the longitudinal and transverse horizontal dispersivity.


*Keywords:* Dispersion; Stochastic continuum model; Fractured rock

* Corresponding author. Tel.: +1-505-844-2450; fax: +1-505-844-7354.
*E-mail addresses:* samcken@sandia.gov (S.A. McKenna), ddwalker@uiuc.edu (D.D. Walker), bwarnol@sandia.gov (B. Arnold).
[1] Current Address: Illinois State Water Survey, 2204 Griffith Dr., Champaign, IL 61820, USA.

0169-7722/02/$ - see front matter 
doi:10.1016/S0169-7722(02)00189-4

## 1. Introduction

Dispersion in groundwater transport systems can be defined as the occurrence and evolution of a transition zone between two domains of the fluid phase with different compositions. For example, the transition zone between the concentration of a continuous contaminant source and the ambient concentration of the groundwater. This definition does not imply any specific process through which this transition zone comes into being, nor does it imply a specific scale for this transition zone. Dispersivity is the rate of change of the second spatial moment of the concentration, and it is generally calculated along the principal axes of the flow system. Along each principal axis, the dispersivity can be considered as a characteristic length of the transition zone between the two domains of the fluid phase.

At Yucca Mountain, dispersion of radionuclides in the saturated zone (SZ) is a key process in determining the long-term performance of the repository. Calculations done to assess the future performance of the potential repository (e.g., Arnold, 2000) employ a model of dispersion that is based on deviations along and transverse to the mean flow direction drawn from Gaussian distributions. An extension of this Gaussian model provides an analytical solution for the dispersion of a solute that has been successfully applied to a number of field studies with less heterogeneous permeability fields than those observed at Yucca Mountain. This Gaussian model is currently used to describe the small-scale dispersion that occurs within single elements of a much larger site-scale model (Zyvoloski et al., 2003). Several questions remain regarding the application and limitations of the Gaussian model in describing longitudinal and transverse dispersion in the fractured rocks at Yucca Mountain. Additionally, the introduction of radionuclides at the surface of the SZ may occur as a distributed or focussed source and the effect of these different geometries must be considered in the large-scale performance assessment (PA) model.

Despite the importance of the dispersion process, little experimental data are available to estimate the longitudinal and transverse dispersivities at Yucca Mountain. In order to better constrain the possible values of dispersivity at Yucca Mountain, an expert elicitation (Geomatrix Consultants, 1998) was conducted to elicit distributions of longitudinal and transverse dispersivities, along with distributions of other SZ parameters, from a panel of experts. The expert panel was provided with all available information on the SZ at Yucca Mountain as well as numerous presentations by the SZ data collection and modeling teams and then asked to provide probability distributions of several hydrological parameters based on their broad experience and the site-specific Yucca Mountain data. One member of the expert panel provided asymptotic estimates of the longitudinal and transverse dispersivity values after 30 km of travel. Additionally, the expert elicitation process resulted in two strong recommendations to better define dispersivity for the SZ at Yucca Mountain: (1) conduct a kilometer scale tracer test to provide direct measures of dispersivity at a scale that is pertinent to the performance assessment calculations; and (2) conduct a series of high-resolution, stochastic flow and transport simulations to assess the amount of dispersion that could occur within a single gridblock of the large-scale SZ model. This second recommendation is the motivation and purpose of the work presented here.

The objective of this analysis is to use high-resolution stochastic continuum models to estimate the transverse and longitudinal dispersion that may occur at the sub-gridblock scale within the SZ site-scale model. Existing data are employed as the basis for two different conceptual models of fracture permeability at the sub gridblock scale. Two different source geometries, point and distributed planar, are employed to simulate different potential source terms. This analysis explicitly applies only to that part of the SZ flowpath that is located within the fractured rocks of the middle volcanic aquifer in the SZ down-gradient from and beneath the potential repository. Estimates of dispersivity derived from this analysis are compared to estimates of dispersivities derived from the expert elicitation and from analytical solutions; the resulting estimates can be used directly, in PA calculations.

## 2. Stochastic modeling of fracture permeability

A stochastic continuum model (SCM) is used to represent the fracture permeability in the middle volcanic aquifer in the SZ down-gradient of the potential repository. The SCM approach has been used previously to model fracture systems at experimental facilities for nuclear waste programs in the US (see Altman et al., 1996) and in Sweden (Follin and Thunvik, 1994; Tsang et al., 1996). In these studies, geostatistical simulation algorithms were used to model continuum properties of discrete fracture systems at the scale of numerical flow and transport model gridblocks (1s to 10s of meters). A similar approach constrained by the available data at Yucca Mountain is applied herein. All fracture permeability models are created within a three-dimensional domain that is representative of a single gridblock (element) within the SZ site-scale model (Zyvoloski et al., 2003). The dimensions of the domain are $496 \times 496 \times 48$ m and the domain is discretized into $4 \times 4 \times 2$-m gridblocks for a total of 369,024 elements.

### *2.1. Available data*

The available data exist as observations of discrete fractures made on outcrops and in the Exploratory Studies Facility (ESF) and as direct measurements of fracture permeability at the Yucca Mountain site. Mapping studies in boreholes, and the ESF suggest a dense, well-connected set of fractures, with approximately 89% of the fractures in the range of 0.3–3 m in length, and approximately 1% greater than 10 m. Fracture spacings tend to be on the same order as fracture lengths, i.e., fractures of 10-m length tend to be spaced 10 m apart. This spacing information, coupled with a range of fracture orientations, suggests that the fractures are well-connected over a range of length scales (Sonnenthal et al., 1997). Borehole data and line surveys indicate that, after correcting for dip, the geometric mean fracture spacing is 0.25 m for all fractures (Table 6; Kuzio, 2000). Fracture observations made by Sweetkind and Williams-Stroud (1996) show that given the limits of observation on the outcrops and in the ESF, the distributions of fracture length may be either exponential or power-law. Orientations of fractures observed by Sweetkind and Williams-Stroud (1996) cover a range of azimuths from the northeast to northwest and are generally steeply dipping (near vertical).

A number of studies in fractured rock aquifers have shown that groundwater flow often occurs in just a small fraction of the available fractures (see Hsieh, 1998; Tsang et al., 1996). Borehole flowmeter surveys at Yucca Mountain indicate that discrete intervals of the aquifer have flow rates that are significantly greater than the remainder of the aquifer. The dip-corrected, geometric mean spacing of these flowing intervals is 19.7 m (Kuzio, 2000). Single-well, double-packer tests have been conducted throughout the middle volcanic aquifer, and multi-well interference tests have been conducted in a number of the identified flowing intervals (Arnold, 1998). The log permeability distributions of these tests overlap, suggesting that some of the single-well test results represent the more conductive flowing intervals (Arnold, 1998; Figs. 8–27). The natural log variance of the pooled permeability data set is 9.5. The minimum log permeability of the multi-well tests indicates that the log10 permeability threshold for flowing features is approximately $-12.2$ $m^2$. The permeability data demonstrate an empirical cumulative distribution function (cdf) typical of a weakly bimodal distribution (Fig. 1), similar to that used in the UZ studies of Tsang (1997).

A specific set of hydraulic tests conducted at the C-well complex southeast of the proposed repository indicate that the highly transmissive zones are due to discrete zones of enhanced fracturing (Geldon, 1996). Hydraulic testing at the C-well complex has also indicated the presence of large-scale (up to several kilometers) high-permeability features. In the vicinity of the C-well complex, these features are associated with observed faults (Geldon et al., 1997).

### 2.2. Background permeability model

The field observations and lithology of the middle volcanic aquifer indicate a medium dominated by fracture flow with strong anisotropy (major axis aligned north–south) and

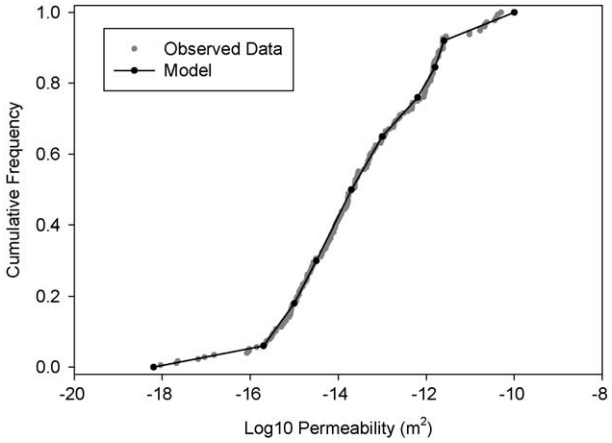


Fig. 1. Cumulative distribution of observed log10 permeability measurements (Arnold, 1998) and the model used to describe the cumulative distribution within the geostatistical simulation algorithm. The 10 permeability threshold values of the model are shown as solid black circles.

subvertical dip directions. The fracturing appears to be sufficiently dense and interconnected that it exhibits a weakly scale-dependent behavior, similar to a stochastic continuum (Tsang, 1997). These characteristics suggest simulating the middle volcanic aquifer as an anisotropic permeability field, with separate classes of spatial continuity to represent the flowing features and the surrounding rock, respectively.

Indicator geostatistical simulation uses the empirical cdf of the data to develop a discrete, nonparametric, three-dimensional model of the permeability. The full distribution of permeability, shown in Fig. 1, is defined at 10 discrete thresholds for the geostatistical modeling (Table 1). Ten thresholds were chosen to provide an accurate match to the distribution of observed data (compare the model to the data in Fig. 1) and to minimize the size of ergodic fluctuations away from the observed cdf in the resulting geostatistical realizations. Additionally, 10 thresholds allow for flexibility in modeling the anisotropy of the permeability correlation structure across the range of the observed permeability values. At each permeability threshold of the input cdf (Fig. 1), a separate spatial correlation function has been defined and is modeled as a variogram. The variogram range represents the continuity of features at that threshold. For media with preferentially oriented fractures, the major axis of variogram anisotropy corresponds to the fracture plane. This study uses the *sisim* (version 2.0) routine, from the GSLIB package (Deutsch and Journel, 1998) to create the background fields of log10 permeability. The empirical cdf for log permeability is inferred from the pooled single-well and multi-well hydraulic test data (Fig. 1). The minimum log10 permeability of the multi-well hydraulic tests, $-12.2$ $m^2$, is used as the permeability threshold between background and large-scale fractures.

This study uses the observed fracture lengths and flowing interval spacings to set variogram ranges, using the relationship that the integral scale of the exponential variogram model is equal to the average length of simulated features. For cutoffs below the critical value of $-12.2$ log10 $m^2$, flow is assumed to be dominated by the permeability resulting from the majority of fractures (lengths less than 3 to 4 m) (Sweetkind and Williams-Stroud, 1996). For these fractures, the variogram integral scale is set to 4 m in

Table 1
Parameters describing the indicator variogram models used to build the background fracture permeability simulations

| Threshold permeability (log10 ($m^2$)) | cdf Value at threshold | Nugget | Sill | Effective range ( *Y*-direction) (m) | Anisotropy (*X*:*Y*:*Z*) |
|---|---|---|---|---|---|
| − 18.2 | 0.00 | NA | Minimum | NA | NA |
| − 15.7 | 0.06 | 0.0 | 0.056 | 12 | 3:12:12 |
| − 15 | 0.18 | 0.0 | 0.148 | 12 | 3:12:12 |
| − 14.5 | 0.30 | 0.0 | 0.210 | 12 | 3:12:12 |
| − 13.7 | 0.50 | 0.0 | 0.250 | 12 | 3:12:12 |
| − 13 | 0.65 | 0.0 | 0.228 | 12 | 3:12:12 |
| − 12.2 | 0.75 | 0.0 | 0.182 | 60 | 25:60:60 |
| − 11.8 | 0.85 | 0.0 | 0.131 | 60 | 25:60:60 |
| − 11.6 | 0.92 | 0.0 | 0.074 | 60 | 25:60:60 |
| − 10 | 1.00 | NA | Maximum | NA | NA |

An exponential model is specified for all variograms.

the plane of the fracture (i.e., an exponential variogram with effective range of 12 m). The thickness of such fractures (in the *X*-direction) is on the order of millimeters, which can be represented by making the adjacent blocks within a finite element model uncorrelated by setting the effective range perpendicular to the fracture plane to be less than the grid scale of 4 m. The theoretical sill of each variogram is calculated as $p(1-p)$ where $p$ is the proportion of values less than or equal to the current indicator threshold.

The log10 permeabilities above $-12.2$ represent the flowing fractures as planar features oriented north–south (*Y*-direction) with subvertical dips and spacing approximately equal to length. This study uses an integral scale of 20 m in the plane of the flowing fractures based on the interpretation of an exponential or power-law distribution to define the fracture lengths (Sweetkind and Williams-Stroud, 1996, Fig. 21). Available data suggest a mean width of approximately 8 m for the flowing features (Kuzio, personal communication) and the variogram in the width, (*X*) direction, has a range of 25 m. The variogram parameters for all the log10 permeability thresholds are given in Table 1. An example background fracture permeability realization is shown in Fig. 2A.

### 2.3. Enhanced permeability model

The enhanced permeability model overlays a set of discrete, conductive objects onto the background model of permeability. These discrete objects represent the large features observed in the field such as the high-permeability connections inferred between the C-well complex and boreholes USW H-4 and UE-25 WT#14 (Geldon et al., 1997). These long features are also consistent with the power-law distribution of fracture lengths suggested by the fracture mapping studies. The objects are conceptualized as randomly located, disk-shaped fractures, created via Boolean simulation (e.g., Schmitt and Beucher, 1997).

A small number of domain-spanning features are simulated as disks with a length that is equal to or larger than the model domain length. The locations of the disk centers are purely random and independent (i.e., a Poisson process) and constrained to a frequency of less than 2% of the domain. The feature centers can lie outside the simulation domain such that only portions of the disks appear within the domain with orientations drawn from a normal distribution with a mean orientation of 0° (North) and a standard deviation of 15° (see example in Fig. 2B). These boolean features are mapped onto the background permeability simulation (Fig. 2C) assuming a constant permeability of $1 \times 10^{-11}$ m$^2$ independent of the background model permeability at that location. This permeability corresponds, approximately, to the 95th percentile of the measured permeability values as shown in Fig. 1.

For both conceptual models, a total of 50 fracture permeability realizations are created and evaluated to determine the reproduction of the observed fracture and permeability

Fig. 2. Example realization of the background fracture permeability conceptual model (A). Example of large-scale features created using boolean simulation (B) and example realization of the feature-based conceptual model of fracture permeability (C). The large-scale features are assigned a constant log10 permeability of $-11.0$ m$^2$. The final "enhanced" model of permeability shown in image C is created by combining the geostatistical simulation of background permeability (A) with the boolean simulation of features in the image B. The color legend indicates log10 permeability in m$^2$.

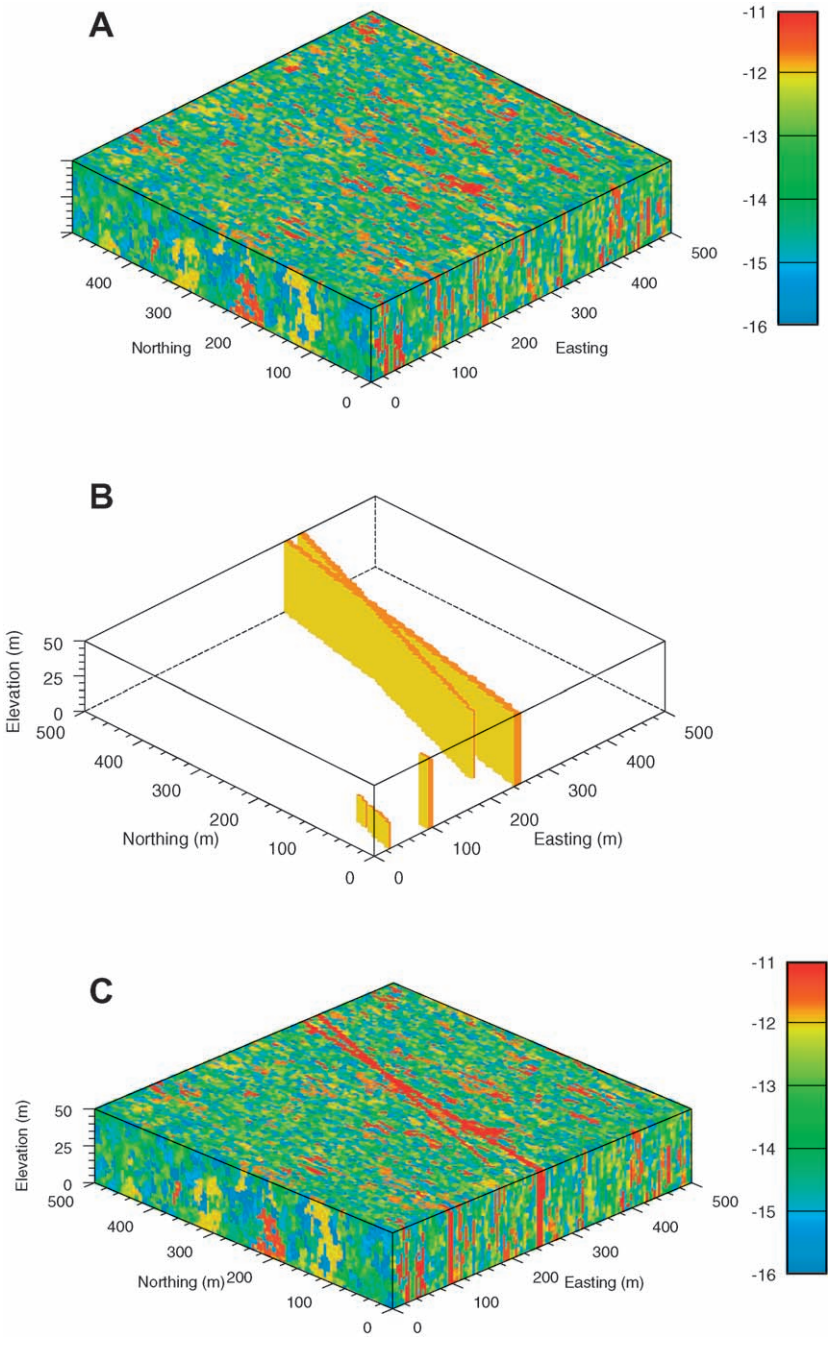
A
-11
-12
-13
-14
-15
-16
400
300
Northing
200
100
0
0
100
200
Easting
300
400
500
B
Elevation (m)
50
25
0
500
400
300
Northing (m)
200
100
0
0
100
200
Easting (m)
300
400
500
C
Elevation (m)
50
25
0
500
400
300
Northing (m)
200
100
0
0
100
200
Easting (m)
300
400
500
-11
-12
-13
-14
-15
-16

characteristics. The average spacing between high-permeability regions in the realizations compares well with the observed spacing (20 m) between flowing features. The simulated permeability distributions also reproduce the observed permeability distribution (see McKenna and Walker, 2000).

## 3. Flow and transport modeling

In the preceding section, we inferred two stochastic continuum models for the heterogeneous fracture permeability in the SZ. The first model defines permeability resulting from a dense network of small isotropic fractures, with longer, more conductive fractures oriented north–south. The second model adds a small set of randomly located, very long features with a mean north–south orientation. In this section, groundwater flow and tracer transport are simulated through multiple realizations of the two permeability models to evaluate the amount of dispersion in a single SZ site-scale model numerical gridblock. For each permeability realization, a steady-state groundwater flow field is determined and particle tracks along streamlines are simulated. The particle tracking used only considers advection and no random perturbations are added to account for fine scale dispersion nor are the effects of molecular diffusion modeled. Therefore, dispersion is due solely to the spatial variability in the groundwater velocity field. The finite element model, FEHM (Zyvoloski et al., 1997) is used for both the flow solution and the particle tracking. Two different source zone geometries are considered to examine different scenarios of transport from the repository to the water table.

### 3.1. Boundary and source zone conditions

The boundary conditions are set to fixed head values on the two ends of the domain and to no-flow boundaries on the sides of the model domain (Fig. 3). The head difference

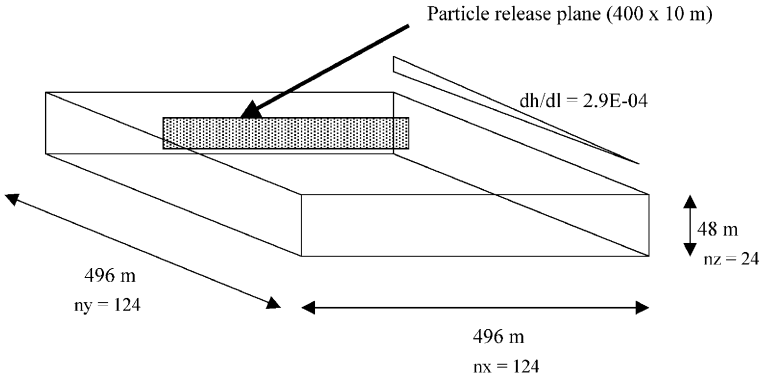


Fig. 3. Schematic diagram of the flow and transport model setup. The top, bottom and sides of the model are no-flow boundaries and the ends of the model are set with fixed heads to impose the mean gradient. Particles are released from a plane or from a single gridblock within the plane.

across the model domain is based on the average value of the gradient along the direction of the most likely flowpath in the SZ site-scale model. This gradient is $2.9 \times 10^{-04}$ and is within the range of gradients presented by Luckey et al. (1996).

The first conceptual model of the source geometry is a planar source as adapted from the streamtube model of the contaminant plume employed in TSPA-VA (Arnold, 1998) where each streamtube was associated with a different region of the repository footprint. In the TSPA-VA, each streamtube represents the radionuclide flux resulting from multiple canister failures in each region of the repository. The planar source implementation in this study assumes that the source zone is 400 m wide by 10 m high and is centered within the model domain. Within the source plane, the density of particle release locations is proportional to the groundwater flux through an individual element as opposed to the uniform source distribution used in TSPA-VA.

The second conceptual model of the source is that of a point release. This more conservative source model corresponds to a single canister release in the unsaturated zone or strong channeling (focusing) of flow within the unsaturated zone from a number of canister releases. Under this scenario, all of the particle release points are within a single numerical gridblock. The gridblock chosen for the particle release points is that with the highest groundwater flux that also lies within the $400 \times 10$-m plane used as the planar source. For both source geometries, a total of 4000 particles were tracked throughout the model.

### 3.2. Dispersivity calculations

Wen and Gomez-Hernandez (1998) examined two-dimensional transport in heterogeneous fields with particle tracking. This approach, extended to the three-dimensional case, represents the solute plume by a finite set of particles tracked along streamlines. In this situation, the dispersivities are defined in terms of the change in second moments, $X_{11}$, $X_{22}$, $X_{33}$, of the particle trajectories with respect to time (after Wen and Gomez-Hernandez, 1998):

$$\alpha_L(t) = \frac{1}{2U}\frac{dX_{11}}{dt} \quad \alpha_H(t) = \frac{1}{2U}\frac{dX_{22}}{dt} \quad \alpha_V(t) = \frac{1}{2U}\frac{dX_{33}}{dt} \tag{1a, b, c}$$

where $t$ is time, $U$ is the arithmetic mean particle velocity, $\alpha_L$ is the longitudinal dispersivity, $\alpha_H$ is the horizontal transverse dispersivity and $\alpha_V$ is the vertical transverse dispersivity. Apparent macrodispersivities are those determined from a single measurement of the particle trajectories at time $t$. These macrodispersivites are given, for an instantaneous injection boundary condition, as (after Wen and Gomez-Hernandez, 1998):

$$\alpha_L(t) = \frac{X_{11}(t)}{2Ut} \tag{2a}$$

$$\alpha_H(t) = \frac{X_{22}(t)}{2Ut} \tag{2b}$$

$$\alpha_V(t) = \frac{X_{33}(t)}{2Ut} \tag{2c}$$

The longitudinal and transverse dispersivities are calculated from the particle travel times and the transverse displacements of the particles between the release points and the location where each particle crosses a down-gradient "collection" plane oriented normal to the mean flow direction. For this model setup and a flux-weighted, instantaneous injection of particles, Kreft and Zuber (1978) present an analytical solution for the longitudinal dispersivity:

$$\alpha_L = \frac{x}{2}\left(\frac{\sigma_t(x)}{m_t(x)}\right)^2 \tag{3}$$

where $m_t(x)$ and $\sigma_t(x)$ are the mean and standard deviation of the travel times at travel distance of $x$. Outliers in the travel time distribution can cause large fluctuations in the calculated value of $\alpha_L$ between realizations. The log transform of the travel times is used to mitigate the effect of these outliers. Statistics based on the log values of the travel times are much less sensitive to outliers than are those calculated with the raw travel times (Khaleel, 1994; Wen and Gomez-Hernandez, 1998). The expressions for the mean and standard deviation of the travel time distribution in Eq. (3) are now determined as:

$$m_t(x) = \exp[m_{\ln\ t}(x) + \sigma^2_{\ln\ t}(x)/2] \tag{4a}$$

$$\sigma^2_t(x) = m^2_t(x)[\exp(\sigma^2_{\ln\ t}(x)) - 1] \tag{4b}$$

where $m_{\ln\ t}(x)$ and $\sigma^2{}_{\ln\ t}(x)$ are the mean and variance of the natural log travel times at a travel distance $x$.

The growth of the second moment of the plume in the transverse directions is difficult to derive from the particle tracking results, especially in a strongly heterogeneous medium. Therefore, the variances of the transverse displacements of the particles are used as a proxy for the transverse second moments of the plume, $X_{22}$ and $X_{33}$, presented in Eqs. (2b) and (2c). The transverse dispersivities are calculated as:

$$\alpha_H(x) = \frac{\psi_{22}(x)}{2x} \tag{5a}$$

$$\alpha_V(x) = \frac{\psi_{33}(x)}{2x} \tag{5b}$$

where $\psi_{22}(x)$ and $\psi_{33}(x)$ are the *variances of the differences* between the transverse particle travel position at travel distance $x$ and the initial traverse coordinate at the source location for the transverse $X$ (horizontal) and $Z$ (vertical) positions, respectively. This approximation has been used previously to evaluate transverse dispersion (Follin and Thunvik, 1994; Wen and Gomez-Hernandez, 1998).

For transport in a three-dimensional field with a flux weighted source boundary condition, Dagan (1988, Eqs. (24) and (38)) gives the following analytical expressions for the second moments of the plume as a function of normalized time:

$$X_{11}(t') = \sigma_Y^2 \lambda^2 \left[ 2t' - \left( \frac{8}{3} - \frac{4}{t'} + \frac{8}{t'^3} - \frac{8}{t'^2} \left( 1 + \frac{1}{t'} \right) e^{-t'} \right) \right] \tag{6}$$

$$X_{22}(t') = X_{33}(t') = \sigma_Y^2 \lambda^2 \left[ 2 \left( \frac{1}{3} - \frac{1}{t'} + \frac{4}{t'^3} - \left( \frac{4}{t'^3} + \frac{4}{t'^2} + \frac{1}{t'} \right) e^{-t'} \right) \right] \tag{7}$$

where $\sigma_Y^2$ is the variance of the ln $K$ field with isotropic spatial correlation of integral length $\lambda$ (practical range = $3\lambda$), and $t' = X/\lambda$ is the dimensionless time, or displacement. Combining Eqs. (2a,b and c) with Eqs. (6) and (7) gives analytical expressions for the macrodispersivities as a function of time. It is noted that the permeability fields used here differ from those specified in the development of Eqs. (6) and (7) as the natural log variance is higher, at 9.5, than the theoretical limit of 1.0 and that the fields are not ergodic nor isotropic. Differences between analytical results and numerical results are compared below.

## 4. Results

Longitudinal, $\alpha_L$, transverse horizontal, $\alpha_H$, and transverse vertical dispersivities, $\alpha_V$, were determined for each of the 50 background and 50 enhanced fracture permeability models using both the "point" and "planar" source geometry. For each directional dispersivity, the results are shown as a plot of the median dispersivity value (meters) determined across the 50 realizations as a function of absolute travel distance (Fig. 4). The analytical solutions as a function of travel distance, Eqs. (6) and (7), are shown in Fig. 4A and B for ln $\sigma^2$ of 1.0 and 9.46, respectively. Travel distance is defined as the distance from the source to each of the nine different collection planes (Table 2). Also shown in Fig. 4, by arrows, are the expert elicitation estimates of dispersivity after a travel distance of 30 km.

### *4.1. Longitudinal dispersivity*

Longitudinal dispersivity is calculated from the coefficient of variation of the travel time distribution as measured at each collection plane (Eq. (3)). The numerical results for the two different conceptual models and the two different source terms are shown in Fig. 4C,D. The most notable aspect of Fig. 4C is the extreme values of dispersivity that occur with the enhanced permeability model and the planar source. These values are approximately an order of magnitude higher than the values for the background model with either source geometry or for the same enhanced model with the point source.

These extreme results are interpreted as being due to some realizations producing a strongly bimodal distribution of travel times while others do not. Those realizations with high-permeability features that can capture a significant fraction of the particles along the

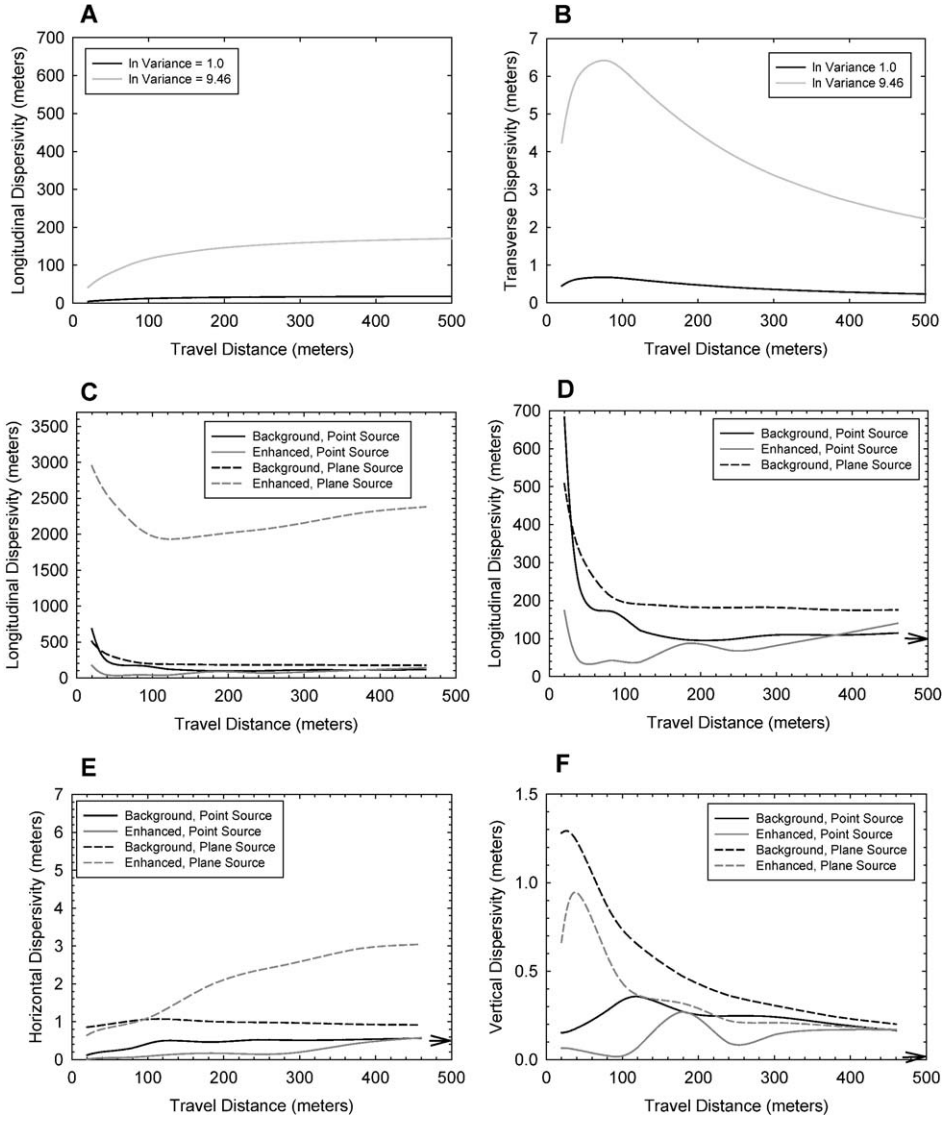


Fig. 4. Dispersivity as a function of travel distance for the analytical models and the numerical results. The longitudinal and transverse dispersivities as calculated with the analytical model are given in (A) and (B), respectively. The longitudinal dispersivity as calculated numerically is given in (C) and (D) (D is an expanded view of C). The numerical results for horizontal transverse and vertical transverse dispersivity are shown in (E) and (F), respectively. The arrows in (D), (E) and (F) indicate the final (30-km travel length) value of the dispersivities from the expert elicitation.

flowpath will have larger longitudinal dispersivities than those that do not. An example of this behavior is shown in Fig. 5 where the background permeability model (Fig. 5A and B) shows transport distances for the first 50 days (blue symbols) to be generally less than half

Table 2
Travel distances for the dispersivity calculations

| Collection plane | Absolute travel distance (m) | Relative travel distance (number of correlation lengths) |
|---|---|---|
| 1 | 20.0 | 1.0 |
| 2 | 40.0 | 2.0 |
| 3 | 80.0 | 4.0 |
| 4 | 120.0 | 6.0 |
| 5 | 180.0 | 9.0 |
| 6 | 240.0 | 12.0 |
| 7 | 300.0 | 15.0 |
| 8 | 380.0 | 19.0 |
| 9 | 460.0 | 23.0 |

The relative distances are calculated as: (absolute travel distance )/$\lambda$ where $\lambda$ is set to the model input value of 20.0 m.

the domain distance. When a high-permeability feature is added to create the enhanced model, a large fraction of the particles are transported across the entire model domain in 50 days or less (compare the locations of the blue symbols in Fig. 5A and B to those in Fig. 5C and D). The high-permeability feature geometry that is best suited for capturing the flowpaths is a feature that has an oblique orientation to the principal flow direction. For the point source geometry, the high-permeability features create channels of high flux and all of the particles are assigned starting locations within that channel resulting in dispersivities that are considerably smaller than those calculated for the planar source geometries on the same permeability realization. However, as seen in the results shown in Fig. 5D, there can be considerable velocity variation across the single element chosen for the particle starting locations.

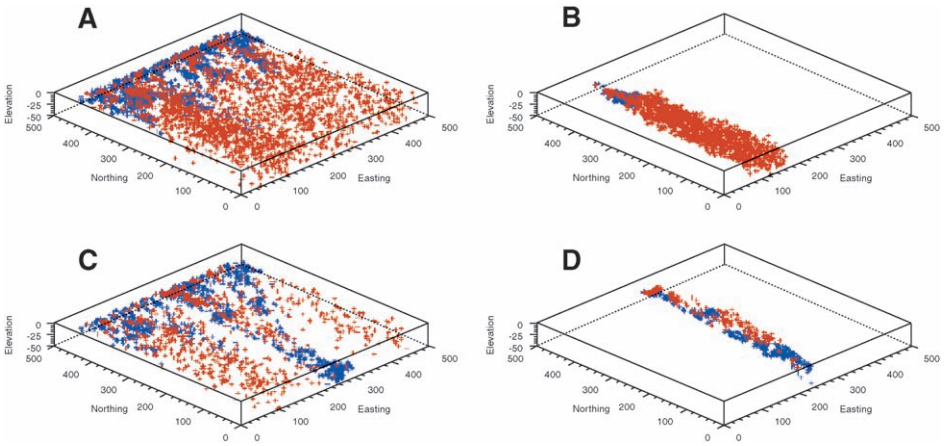


Fig. 5. Example particle locations at 50 days (blue) and 500 days (red) after release for realization number 7. Results for the background permeability model are shown for the planar source (A) and the point source (B). Results for the enhanced permeability model are shown for the planar source (C) and the point source (D).

The results in Fig. 4C,D also show decidedly non-Gaussian behavior in that dispersivity is highest at short travel distances and then asymptotically decreases to a final value at large travel distances. This behavior is contrary to the trend of the analytical solution (Fig. 4A). This high dispersivity at short distances is attributed to the large spatial variability of the fracture permeability models, which channel the groundwater flux into discrete zones (e.g., Tsang and Neretnieks, 1998) to a greater degree than the lower variance Gaussian-based permeability models inherent in the analytical solutions. This partitioning of flux creates large variability in groundwater travel times and thus large calculated dispersivities. An example of this short time behavior is shown in Fig. 5A where the particle locations at 50 years (blue symbols) are not well mixed and exhibit channelized transport. As the travel distance increases, the streamlines spread over a larger proportion of the model domain (red symbols in Fig. 5A), the travel times exhibit less overall variability.

Fig. 4D shows Fig. 4C using an expanded vertical scale. From Fig. 4D, the asymptotic values of longitudinal dispersivity for these combinations of permeability model and source geometry all fall within the 110–180-m range. These dispersivities are roughly 24% to 39% of the travel distance. The results for the two different source geometries in the background permeability models appear to have reached an asymptote; however, the dispersivities calculated with the enhanced permeability model appear to still be rising after 460 m of travel (Table 3).

These results can be compared to results obtained from modeling tracer experiments at the C-wells complex. Three different sets of results have been obtained from tracer tests done between boreholes UE-25C #2 and UE-25C #3. The straight-line distance between the boreholes is roughly 30 m with interpreted dispersivity values of 1.9 to 2.6 m (Geldon et al., 1997) and 2.4 to 2.6 m (Fahy, 1997) or roughly 6% to 9% of the travel distance. In terms of absolute values and percentage of travel distance, the longitudinal dispersivities derived from the tracer tests are all less than the values derived from this numerical study. A reason for this difference may be that transport between the two C-wells is thought to occur in only two to three discrete fracture pathways, while flow in the numerical studies presented here occurs throughout the fracture network. Another difference between the results is that the flow field for the tracer tests is radially convergent, while the numerical models use a uniform flow field. Analysis of the effects of the different flow fields and dispersivity is beyond the scope of this study.

Table 3
Calculated dispersivity values at 460-m travel distance

| Calculation method | Longitudinal dispersivity (m) | Transverse horizontal dispersivity (m) | Transverse vertical dispersivity (m) |
|---|---|---|---|
| Analytical ($\ln \sigma^2 = 9.46$) | 169 | 2.4 | 2.4 |
| Background, point source | 115 | 0.6 | 0.2 |
| Enhanced point source | 140 | 0.6 | 0.2 |
| Background, planar source | 175 | 0.9 | 0.2 |
| Enhanced planar source | 2380 | 3.0 | 0.2 |
| Expert panel | (100) | (0.5) | (0.005) |

For the numerical results, the median value across 50 realizations is given. The estimates from the expert panel, given in parentheses, are for a travel distance of 30 km.

### 4.2. Horizontal transverse dispersivity

Horizontal transverse dispersivity is calculated from the variance of the horizontal displacements of the particles as measured at each collection plane (Eq. (5a)). The results for the two different conceptual models and the two different source terms are shown in Fig. 4E. Similar to the results for longitudinal dispersivity, the results for horizontal transverse dispersivity show that the largest values of dispersivity occur within the enhanced fracture permeability model when the planar source geometry is assumed. When this source is coupled with an enhanced permeability model containing large-scale features with variable orientations (as in Fig. 5C), the possibility of preferential channels developing in these features with significantly different transverse flow directions is increased.

The theoretical behavior for transverse dispersivity is that of a rapid rise to a peak value within a few correlation lengths of travel distance and then a gradual decrease to a dispersivity value of zero (Fig. 4B). The planar source geometry in the background permeability model shown in Fig. 4E reproduces the macroscopic dispersivity behavior predicted by the analytical solutions (Eq. (7) and Fig. 4B). The final values of horizontal transverse dispersivity range from approximately 0.6 to 3.0 m, or approximately 0.1% to 0.6% of the travel distance (Table 3).

### 4.3. Vertical transverse dispersivity

Vertical transverse dispersivity is calculated from the variance of the vertical displacements of the particles as measured at each collection plane (Eq. (5b)). The results for the two different conceptual models and the two different source terms are shown in Fig. 4F. All combinations of conceptual model and source geometry converge to the same final dispersivity value of approximately 0.2 m at a travel distance of 460 m (Table 3). This final dispersivity value is an order of magnitude smaller than that predicted by the analytical solution (Eqs. (2c) and (7)). This result may be due to the small vertical dimension of the numerical model domain. The analytical solutions assume an infinite, unbounded domain that is effectively achieved if the extent of the domain is a minimum of 10 correlation lengths. While the domain meets this relative size constraint in the longitudinal and horizontal transverse directions, it is not met in the vertical transverse direction (only two to three correlation lengths), and thus, the calculated dispersivity values are smaller than those predicted by the analytical solution. However, the values of vertical transverse dispersivity calculated from the numerical models may be more representative of the conditions at Yucca Mountain where the water table acts as a zero-flux upper boundary for solute transport.

## 5. Conclusions

High-resolution permeability models based on data observed at Yucca Mountain and used as the basis for calculating dispersivities show that at early times flow in highly heterogeneous fractured media is not dispersive in the classical sense of stochastic theory where the solute plume grows through Gaussian deviations from the mean flow direction.

Instead, these results indicate that at short travel distances, the highly heterogeneous fracture permeability leads to channelized flow and extremely non-Gaussian behavior. At early times, the analytical expressions developed by Dagan (1988) do not agree with the numerical results that demonstrate extremely non-Gaussian behavior. However, after 460 m, 23 correlation lengths, of travel, the analytical expressions for longitudinal and transverse macrodispersivity are within an order of magnitude of predicting the calculated macrodispersivity values.

The exception to this conclusion is the case of large, continuous high-permeability features existing in the domain. These domain-spanning features represent a scale of heterogeneity that is similar to or equal to the size of the model domain and therefore classical dispersion theory cannot describe these results. In the case of a distributed source coupled with these high-permeability features, both longitudinal and transverse dispersivity will be severely underestimated by the analytical solution or the expert elicitation estimates for the travel distances examined in this study. For these situations, the PA models need to be conducted at a finer scale to capture these high-permeability features.

In general, the numerical estimates of dispersivity may not have reached a final asymptotic value after 460 m of travel distance (23 correlation lengths). However, these calculated values compare favorably with the asymptotic (30-km travel length) dispersivity estimates made by the expert panel (Geomatrix Consultants, 1998). The exception to this observation is the expert panel estimate of the vertical transverse dispersivity that is two orders of magnitude less than the numerically calculated dispersivities and three orders of magnitude less than the analytical solution. The relative longitudinal dispersivity values calculated in this report are larger, approximately 30% of the travel distance, than the values interpreted from the C-well tracer tests, about 6–9% of the travel distance.

Results of this work indicate that due to the channeling nature of the flow system, one-dimensional Lagrangian solute transport modeling along streamlines in the SZ is strongly recommended for performance assessment calculations. When large-scale high-permeability features are absent, longitudinal and transverse horizontal dispersivities are reasonably estimated by the analytical solutions. For these situations, dispersion can be adequately modeled with deviations about the streamlines drawn from Gaussian distributions defined by the dispersivities calculated in this study or obtained from the expert elicitation. The conceptual model of large streamtubes of perfectly mixed solute concentrations existing for considerable length along the saturated zone transport pathway, such as was used in the TSPA-VA, is unrealistic at short times, but may provide a reasonable abstraction of the solute transport at the large-scales (km's) of the PA calculations.

## Acknowledgements

This paper benefited from the comments of two anonymous reviewers. This work was supported by the Yucca Mountain Site Characterization Office as part of the Civilian Radioactive Waste Management Program, which is managed by the US Department of Energy, Yucca Mountain Site Characterization Project. Sandia National Laboratories is a

multiprogram laboratory operated by Sandia Corporation, a Lockheed Martin Company, for the United States Department of Energy under Contract DE-AC04-94AL85000.

## References

Altman, S.J., Arnold, B.W., Barnard, R.W., Barr, G.E., Ho, C.K., McKenna, S.A., Eaton, R.R., 1996. Flow Calculations for Yucca Mountain Groundwater Travel Time (GWTT-95). SAND96-0819. Sandia National Laboratories, Albuquerque, NM.

Arnold, B.W. (Ed.), 1998. Saturated Zone Flow and Transport. Chapter 8 of Total System Performance Assessment–Viability Assessment (TSPA-VA) Analyses Technical Basis Document. B00000000-01717-4301-00008 REV 01. CRWMS M&O, Las Vegas, NV.

Arnold, B.W., 2000. Input and Results of the Base Case Saturated Zone Flow and Transport Model for TSPA, ANL-NBS-HS-000030 REV00. CRWMS M&O, Las Vegas, NV.

Dagan, G., 1988. Time-dependent macrodispersion for solute transport in anisotropic heterogeneous aquifers. Water Resources Research 24 (9), 1491–1500.

Deutsch, C.V., Journel, A.G., 1998. GSLIB Geostatistical Software Library and User's Guide, 2nd ed. Oxford Univ. Press, New York, NY.

Fahy, M.F., 1997. Dual-porosity analysis of conservative tracer testing in saturated volcanic rocks at Yucca Mountain in Nye County, Nevada. International Journal of Rock Mechanics and Mining Sciences 34 (3–4), 486.

Follin, S., Thunvik, R., 1994. On the use of continuum approximations for regional modeling of groundwater flow through crystalline rocks. Advances in Water Resources 17, 133–145.

Geldon, A.L., 1996. Results and Interpretation of Preliminary Aquifer Tests in Boreholes UE-25c #1, UE-25c #2, and UE-25c #3, Yucca Mountain, Nye County, Nevada. Water-Resources Investigations Report 94-4177. US Geological Survey, Denver, CO.

Geldon, A.L., Umari, A.M.A., Fahy, M.F., Earle, J.D., Gemmell, J.M., Darnell, J., 1997. Results of Hydraulic and Conservative Tracer Tests in Miocene Tuffaceous Rocks at the C-Hole Complex, 1995 to 1997, Yucca Mountain, Nye County, Nevada. Milestone SP23PM3 US. Geological Survey, Denver, CO.

Geomatrix Consultants, 1998. Saturated Zone Flow and Transport Expert Elicitation Project. Deliverable Number SL5X4AM3. CRWMS M&O, Las Vegas, NV.

Hsieh, P.A., 1998. Scale effects in fluid flow through fractured geologic media. In: Sposito, G. (Ed.), Scale Dependence and Scale Invariance in Hydrology. Cambridge Univ. Press, New York, NY, pp. 335–353. Chapter 12.

Khaleel, R., 1994. Scale and directional dependence of macrodispersivities in colonnade networks. Water Resources Research 30 (12), 3337–3355.

Kreft, A., Zuber, A., 1978. On the physical meaning of the dispersion equation and its solutions for different initial and boundary conditions. Chemical Engineering Science 33 (11), 1471–1480.

Kuzio, S., 2000. Probability Distribution for Flow Interval Spacing. ANL-NBS-MD-000003 Rev. 00. CRWMS M&O, Las Vegas, NV.

Luckey, R.R., Tucci, P., Faunt, C.C., Ervin, E.M., Steinkampf, W.C., D'Agnese, F.A., Patterson, G.L., 1996. Status of Understanding of the Saturated-Zone Ground-Water Flow System at Yucca Mountain, Nevada, as of 1995. Water-Resources Investigations Report 96-4077 US. Geological Survey, Denver, CO.

McKenna, S.A., Walker, D.D., 2000. Modeling Sub Gridblock Scale Dispersion in Three-Dimensional Heterogeneous Fractured Media, ANL-NBS-HS-000022 Rev. 01. CRWMS M&O, Las Vegas, NV.

Schmitt, M., Beucher, H., 1997. On the inference of the Boolean Model. Geostatistics Wollongong 1996, International Geostatistics Congress, Wollongong, Australia, September 1996. Kluwer Academic Publishing, Dordrecht, The Netherlands, pp. 200–210.

Sonnenthal, E.L., Ahlers, C.F., Bodvarsson, G.S., 1997. Fracture and fault properties for the UZ site-scale flow model. In: Bodvarsson, G.S., Bandurraga, T.M., Wu, Y.S. (Eds.), The Site-Scale Unsaturated Zone Model of Yucca Mountain, Nevada, for the Viability Assessment. LBNL-40376. Lawrence Berkeley National Laboratory, Berkeley, CA. Chapter 7.

Sweetkind, D.S., Williams-Stroud, S.C., 1996. Characteristics of Fractures at Yucca Mountain, Nevada: Synthesis Report. Administrative Report. US Geological Survey, Denver, CO.

Tsang, C.-F., 1997. Drift Scale Heterogeneous Permeability Field Conditioned to Field Data. Milestone SP331BM4. Lawrence Berkeley National Laboratory, Berkeley, CA.

Tsang, C.-F., Neretnieks, I., 1998. Flow channeling in heterogeneous fractured rocks. Reviews of Geophysics 36 (2), 275–298.

Tsang, Y.W., Tsang, C.F., Hale, F.V., Dverstorp, B., 1996. Tracer transport in an stochastic continuum model of fractured media. Water Resources Research 32 (10), 3077–3092.

Wen, X.-H., Gomez-Hernandez, J.J., 1998. Numerical modeling of macrodispersion in heterogeneous media: a comparison of multi-Gaussian and non-multi-Gaussian models. Journal of Contaminant Hydrology 30, 129–156 (Elsevier, Amsterdam, The Netherlands).

Zyvoloski, G.A., Robinson, B.A., Dash, Z.V., Trease, L.L., 1997. User's Manual for the FEHM Application—A Finite-Element Heat- and Mass-Transfer Code. LA-13306-M. Los Alamos National Laboratory, Los Alamos, NM.

Zyvoloski, G.A., Kwicklis, E., Eddebbarh, A.A., Arnold, B.W., Faunt, C., Robinson, B.A., 2003. The site-scale saturated zone flow model for Yucca Mountain: calibration of different conceptual models and their impact on flow paths. J. Contam. Hydrol. 62-63C, 731–750.